J. Fluid Mech. (2005), *vol.* 536, *pp.* 27–48.
doi:10.1017/S0022112005004787 Printed in the United Kingdom

Turbulence structure in sharp open-channel bends

By K. BLANCKAERT[1] AND H. J. DE VRIEND[2]

[1]ICARE-ENAC, Ecole Polytechnique Fédérale, CH-1015 Lausanne, Switzerland

[2]Delft University of Technology, POB 5048, 2600 GA Delft, The Netherlands

(Received 23 March 2004 and in revised form 7 February 2005)

In spite of its practical relevance, little is known about the turbulence characteristics in sharp open-channel bends, which may largely be attributed to a lack of accurate experimental data. This paper reports an experimental investigation of the turbulence structure in one cross-section of an open-channel bend. The flow pattern in this section is characterized by a bicellular pattern of cross-stream circulation (secondary flow) and, in the outer part, a strongly reduced turbulence activity as compared with straight uniform shear flow. The turbulence structure differs fundamentally from that in straight uniform shear flow. The velocity fluctuations are atypically coherent over the channel width, whence the measured signal is decomposed into slow width-coherent fluctuations and a fast background signal. The width-coherent fluctuations reflect a bulk spatio-temporal oscillation of the pattern of circulation cells whereas the background signal represents developed turbulence. A spectral analysis shows that the width-coherent fluctuations have the characteristics of a wavelike motion, i.e. they contribute significantly to the turbulent normal stresses but only weakly to the shear stress, whereas the background turbulence is characterized by efficient shear stress generation. The reduced turbulence activity and the tendency of the secondary-flow pattern to oscillate are both effects of the streamline curvature. Similar observations on reduced turbulence activity and the tendency to wavelike motion have been reported in literature for flows in curved wind tunnels and density-stratified flows. Our experimental results indicate that these phenomena are potentially important in curved open-channel flows, where they affect the mixing and transport capacity of the flow.

1. Introduction

Most natural rivers follow a winding course in their alluvial plane. Major points of attention in river management are: (i) bank erosion, especially in the outer bends; (ii) transport, spreading and mixing of suspended matter, pollutants, oxygen, biological species, heat, etc.; (iii) transport of sediment and the associated erosion and deposition phenomena. All of these points depend strongly on the turbulence characteristics of the flow. In spite of this practical relevance, little is known about the turbulence characteristics in open-channel bends. Numerical models of flow in open-channel bends frequently use extensions of turbulence closures that were developed for two-dimensional boundary-layer flow. As these closure models take insufficient account of the curvature effects on the turbulence structure, the results are often disappointing. The almost complete lack of experimental data on the turbulence characteristics in

sharply curved open-channel flow hampers the development of improved turbulence models.

Blanckaert & de Vriend (2005) present detailed experimental data on the turbulence characteristics in the outer half of one cross-section of an open-channel bend. The cross-stream flow pattern (secondary flow) in this section consists of two cells rotating in opposite directions. The turbulence activity in most of the outer bend is much less than in straight uniform shear flow. This is attributed to a less efficient generation of turbulence, especially the Reynolds shear stress components. The deviations from the turbulence structure in straight uniform flow are likely to be related to the curvature-flux-Richardson number, which represents the role of the transverse pressure-gradient in analogy to that of density stratification (cf. Bradshaw 1969). In the present paper, the turbulence structure of the same flow field is investigated in more detail. The experiment is described and the main features of the mean flow and the turbulence are presented briefly. We focus on the analysis of the velocity fluctuations, which are decomposed into slow large-scale fluctuations and a rapidly varying background signal. The slow fluctuations are shown to represent an overall oscillation in space and time of the pattern of circulation cells, with the characteristics of a wavelike motion. The relation of this unsteady behaviour to the streamline curvature is investigated. The results are compared with similar findings reported in the literature for flows in curved wind tunnels and density-stratified flows. To our knowledge, observations of these phenomena in open-channel flows have not been reported before.

2. The experiment

River bends exist in nature under a wide variety of spatial scales, planform shapes and hydraulic parameters. As there is no existing experimental set-up that is representative of natural rivers, we have opted for a strongly curved single-bend configuration consisting of a straight inflow reach followed by a bend of constant radius of curvature. The aim was to isolate curvature effects and minimize contamination by upstream geometrical and hydraulic effects. By considering a relatively sharp bend, the curvature effects are more pronounced, and thus better visible.

The experiment was carried out in a laboratory flume of width $B = 0.4\,\mathrm{m}$ and there is a 2 m long straight approach reach, followed by a 120° bend with a constant radius of curvature, R, of 2 m at the centreline. The bottom was covered by a nearly uniform quartz sand with median grain size diameter $d_{50} = 2.1\,\mathrm{mm}$ and density $2650\,\mathrm{kg\,m^{-3}}$. In a preliminary run, the initially horizontal sand bottom was deformed by the flow, via a process of so-called clear-water scour (bed shear stress at or below the threshold of sediment motion). Ultimately, the sediment transport vanished throughout and a stable (zero time derivative) bottom topography that significantly varies in downstream direction was obtained (figure 1). The hydraulic conditions are shown in table 1.

The parameters $R/B = 5$ and $R/H = 17.9$ correspond to a rather tight bend with a high aspect ratio ($B/H = 3.6$). The flume is narrower than usual in natural lowland rivers, but these ratios do occur in mountain rivers and man-made channels. Moreover, the flow in bends with a mobile-bed topography is concentrated in the outer part of the cross-section, where the depth is significantly larger than in the shallow inner bend with its almost 'dead-water' zone (e.g. Odgaard 1984; Dietrich 1987). The flow in the outer bend of the experimental flume is therefore expected to be similar to the flow in the deepest part of wider natural bends.

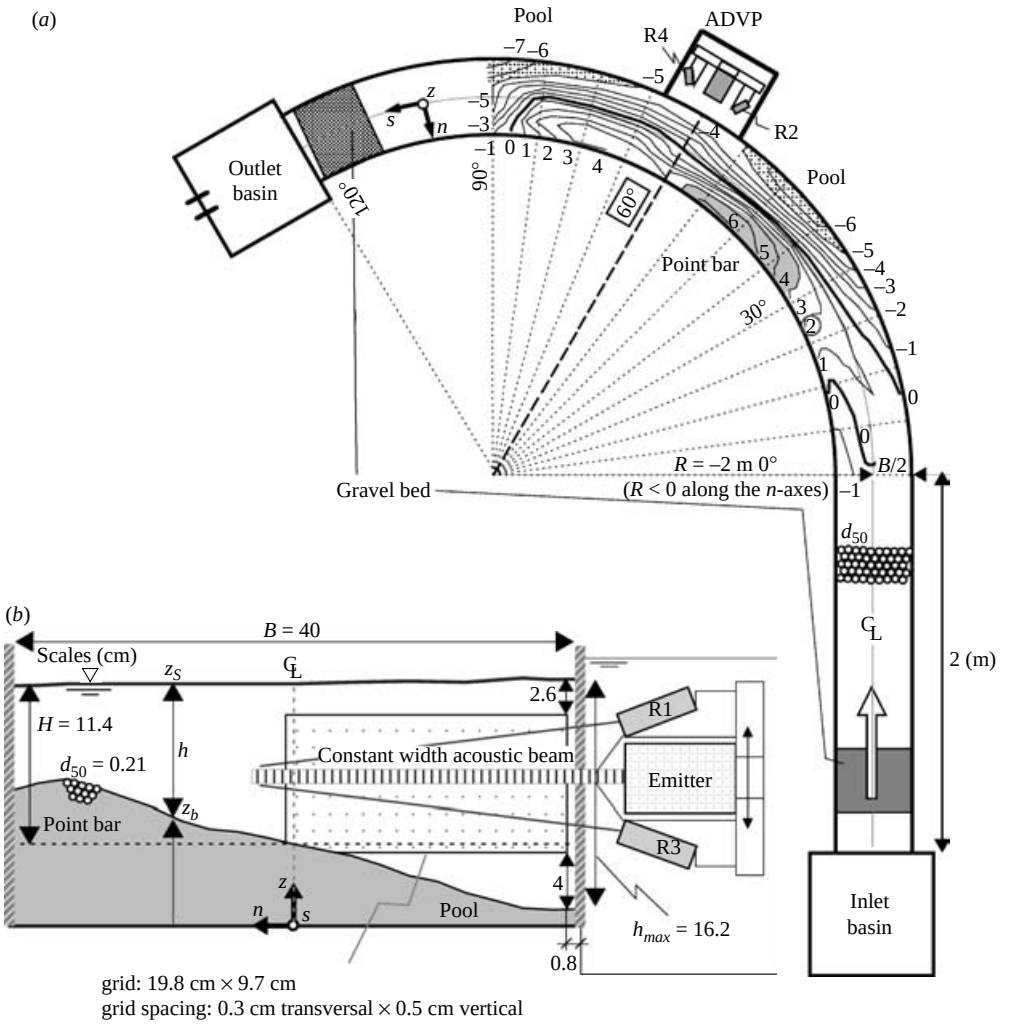

FIGURE 1. (*a*) Experimental set-up, bed topography and reference system. ADVP: central emitter surrounded by four receivers, R1 to R4, placed in a water-filled box attached to the bank. Reference system: ($s - n$), horizontal; z, vertical. Bottom levels (cm) indicated with respect to reach averaged bottom level. (*b*) Measuring grid in cross-section at 60°, ADVP configuration.

Non-intrusive three-dimensional measurements of the mean flow field and the turbulence were made on a fine grid that covers the outer half of one cross-section at 60° from the bend entrance, where downstream variations in the bed topography are minimal (cf. figure 1). By imposing physical boundary conditions (no-slip condition, free shear, etc.) and making use of physical properties of, for example, the turbulent kinetic energy, some experimental data have been extrapolated in the zones close to the water surface and the bed outside the measuring grid, as explained in detail in Blanckaert & Graf (2001). These extrapolations, however, are not essential to the presented analysis.

The data are analysed in a reference system with the s-axis pointing downstream along the channel centreline, the transversal n-axis pointing to the left bank and

R (m)	B (m)	d_{50} (mm)	Q ($\mathrm{l\,s^{-1}}$)	H (m)	S_s (‰)	U ($\mathrm{m\,s^{-1}}$)	C_f (/)	Re (10^3)	Re^* (/)	Fr (/)	R/B (/)	R/H (/)	B/H (/)
−2.0	0.40	2.1	17	0.11	1.89	0.38	0.008	42	70	0.36	5	17.9	3.6

R, centreline radius of curvature (negative along the n-axis)
B, channel width
d_{50}, median grain size diameter of the bed material
Q, flow discharge
H, overall mean flow depth $\approx$ depth at centreline
S_s, overall mean water-surface slope at the centreline
U, overall mean velocity
C_f, friction factor (estimated by Blanckaert & Graf 2001)
τ_b, bottom shear stress, $\tau_b/\rho = u_*^2 = C_f U^2$
$Fr = U/(gH)^{1/2}$, overall mean flow Froude number
$Re_* = u*k_s/\nu$, overall mean particle Reynolds number
ν, molecular viscosity
k_s, Nikuradse equivalent sand roughness

TABLE 1. Hydraulic conditions.

the vertical z-axis directed upward from the horizontal (s, n)-plane (figures 1). The measurements were made with an acoustic Doppler velocity profiler (ADVP), developed at EPFL, which simultaneously measures at a high spatial and temporal resolution the quasi-instantaneous velocity components along a line coinciding with the axis of the instrument. This profiling capacity of the ADVP will be exploited in the present analysis. From the measured data, the mean velocity field, $\boldsymbol{v}(v_s, v_n, v_z)$, as well as the velocity fluctuations, $\boldsymbol{v}'(v_s', v_n', v_z')$, and the turbulent stress tensor, $\overline{v_j' v_k'}$ $(j, k = s, n, z)$, can be evaluated simultaneously along the measuring profile.

The non-intrusive measurements were made by measuring through the Plexiglas outer sidewall of the flume, with the ADVP mounted in a water-filled box attached to the outside of this wall (figure 1). In this configuration, profiles extending over half the channel width were measured every 0.5 cm (figure 1*b*). The sampling frequency was 44.6 Hz and the acquisition time was 180 s. A detailed description of the experimental set-up, the data-treatment procedures and the measuring grid is given in Blanckaert & Graf (2001). More information on the working principle of the ADVP, its experimental uncertainty and its comparison with other velocity meters can be found in Rolland (1994), Lemmin & Rolland (1997), Hurther & Lemmin (1998, 2001), Blanckaert & Graf (2001), Hurther (2001), Blanckaert & de Vriend (2004), and Blanckaert & Lemmin (2005).

In summary, the uncertainty in the mean velocities is estimated at less than 4 %, that in the turbulent normal stresses at less than 10 %, and that in the turbulent shear stresses at slightly less than that. The uncertainty in the turbulence measurements increases progressively towards the fixed boundaries, owing to the steep mean velocity gradient in the measuring volume. The lower 20 % of the boundary layer is affected by it. For that reason, the ADVP measurements focus on the outer-flow region, away from the boundaries.

3. Experimental results

Blanckaert & Graf (2001) gave a detailed presentation of the distributions of all three mean velocity components, as well as all six turbulent stress components.

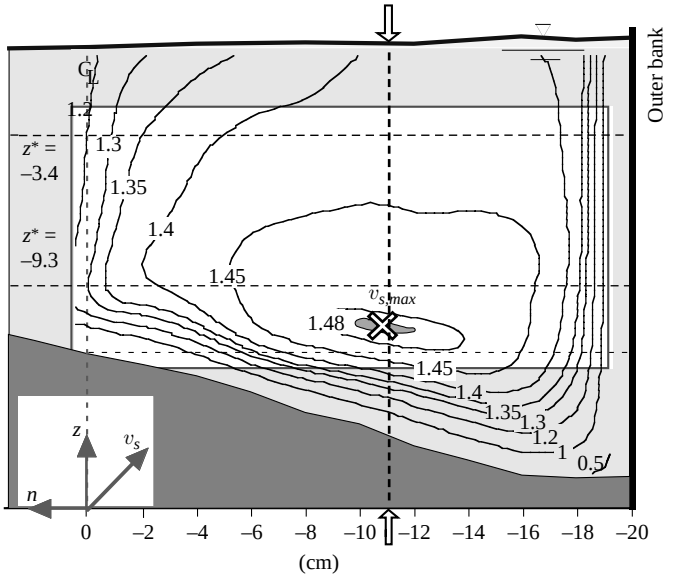

FIGURE 2. Isolines of normalized downstream velocity, v_s/U.

Blanckaert & de Vriend (2005) present and analyse the kinetic energy distribution of the mean flow and the turbulence. The measured data that are of particular relevance to the present paper are briefly summarized below.

The distribution of the normalized downstream velocity component, v_s/U, in the section investigated is presented in figure 2. In a large part of the measuring domain, the downstream velocity is higher than the overall mean velocity of $U = 0.38\,\mathrm{m\,s^{-1}}$. Whilst the maximum velocity in straight uniform flow occurs near the water surface, the maximum in this curved flow is found in the lower part of the water column. The mechanisms leading to this distorted velocity distribution have been investigated by Blanckaert & Graf (2004).

The vectorial representation of the normalized cross-stream motion, $(v_n, v_z)/U$, in the section investigated is shown in figure 3. In the centre region, it shows a circulation cell – termed centre-region cell – with outward velocities near the water surface and inward velocities near the bed. The cross-stream velocities are typically $O(0.1U)$. This cell represents the well-known helical motion that is characteristic of flow in bends. A region characterized by weaker cross-stream velocities, typically $O(0.03U)$, is found close to the outer bank. In the upper part of this outer-bank region an additional circulation cell – termed outer-bank cell – occurs, with a sense of rotation opposite to the centre-region cell. The mechanisms underlying both circulation cells have been investigated by Blanckaert & de Vriend (2003, 2004).

Figures 4(*a*) and 4(*b*) show the normalized distributions of the mean flow kinetic energy, $K/(U^2/2)$, and the turbulent kinetic energy, $k/(u_{*,60}^2/2)$, per unit mass, in which K and k are defined as

$$K = \tfrac{1}{2}\left(v_s^2 + v_n^2 + v_z^2\right), \quad k = \tfrac{1}{2}\left(\overline{v_s'^2} + \overline{v_n'^2} + \overline{v_z'^2}\right), \tag{1}$$

respectively. The characteristic shear velocity in the measuring section, $u_{*,60} = \sqrt{gR_h(-\partial z_{S,60}/\partial s)} = 0.045\,\mathrm{m\,s^{-1}}$, is based on the downstream water-surface gradient at the centreline, $-\partial z_{S,60}/\partial s = 2.89\,‰$, and the hydraulic radius, $R_h = 0.07\,\mathrm{m}$, in the section at 60°. The contributions of the different components to K and k have

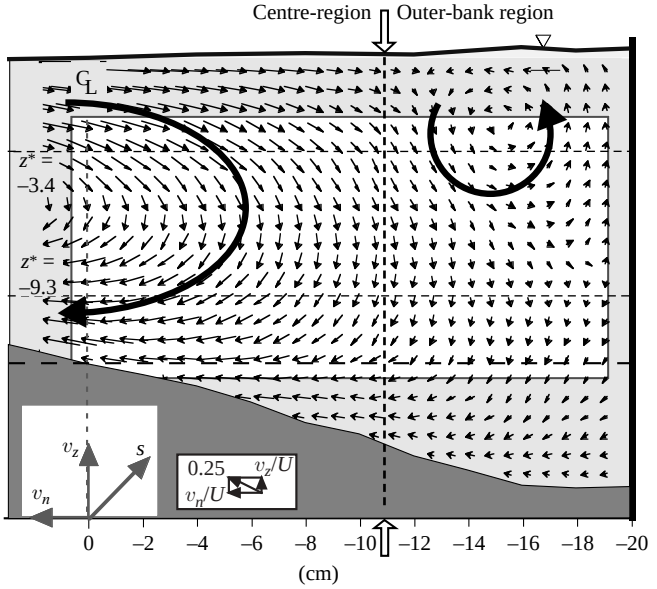

FIGURE 3. Vector-representation of normalized cross-stream motion, $(v_n, v_z)/U$.

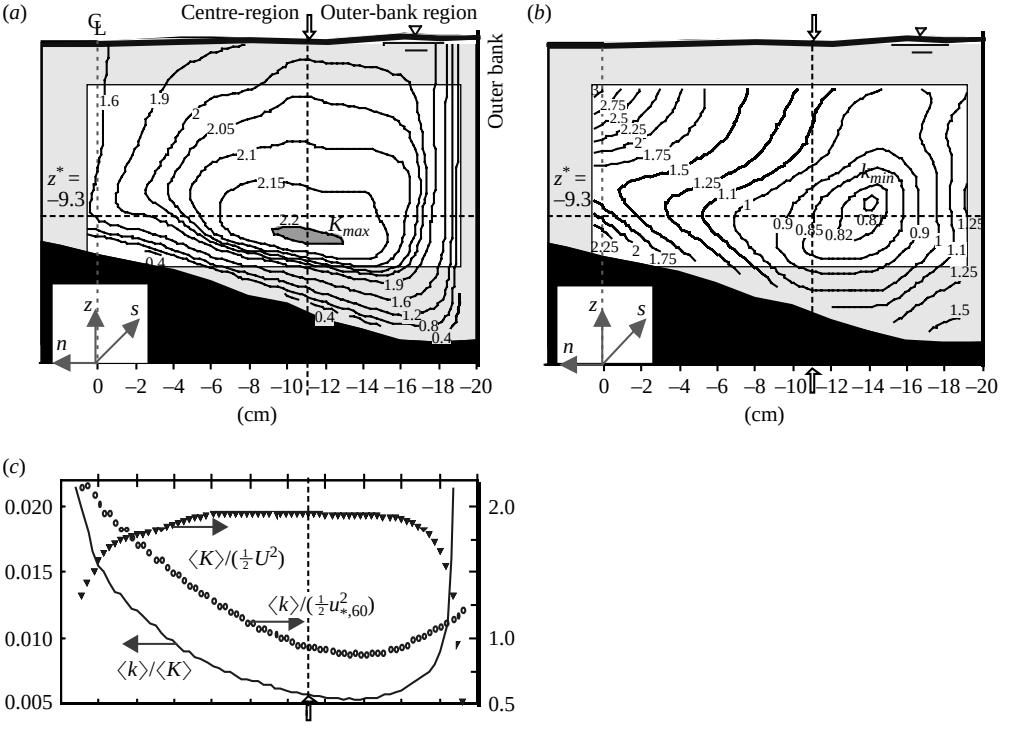

FIGURE 4. (*a*) Isolines of the normalized mean flow kinetic energy, $K/(U^2/2)$; (*b*) Isolines of the normalized turbulent kinetic energy, $k/(u^2_{*,60}/2)$; (*c*) Depth-averaged normalized mean flow and turbulent kinetic energy, $\langle K\rangle/(U^2/2)$, and $\langle k\rangle/(u^2_{*,60}/2)$, and the ratio, $\langle k\rangle/\langle K\rangle$.

been analysed by Blanckaert & Graf (2001). Figure 4(*c*) shows the normalized depth-averaged kinetic energy of the mean flow and the turbulence, $\langle K\rangle/(U^2/2)$ and $\langle k\rangle/(u_{*,60}^2/2)$ respectively, together with the ratio $\langle k\rangle/\langle K\rangle$. Owing to the opposite behaviour of K and k, this ratio exhibits a pronounced variation over the width. Adopting a logarithmic mean-velocity profile and an exponential profile for the turbulent kinetic energy, it is straightforward to show for straight uniform open-channel flow away from banks or sidewalls that $\langle k\rangle/\langle K\rangle$ is constant over the width and depends uniquely on the friction factor, C_f, via (Blanckaert 2002)

$$\langle k\rangle/\langle K\rangle|_{straight} \approx 4.1 C_f. \tag{2}$$

For $C_f \approx 0.008$, this would yield $\langle k\rangle/\langle K\rangle \approx 0.03$. In our curved-flow experiments, the observed value of $\langle k\rangle/\langle K\rangle$ is of the expected order of magnitude near the centreline, but it decreases strongly towards the outer bank, down to $O(0.01)$, to increase strongly in the friction-dominated region very close to the outer bank. Note that the uncertainty in the depth-averaged values increases somewhat towards the outer bank, owing to the necessary extrapolations outside the measuring grid. This uncertainty, however, is too small to explain the difference between the straight-channel values of $\langle k\rangle/\langle K\rangle$ and the measured ones and therefore does not alter our conclusions.

Blanckaert & de Vriend (2005) analyse the mechanisms leading to these distribu tions of k and $\langle k\rangle/\langle K\rangle$. They evaluate the turbulence-structure parameters $a_1 = \sqrt{\overline{v_s'v_z'}^2 + \overline{v_n'v_z'}^2}/2k$ and $\nu_{jk} = \nu_{kj} = -(\overline{v_j'v_k'} - 2/3\delta_{jk}k)/2e_{jk}$, in which δ_{jk} is the Kronecker delta and e_{jk} are the strain rates, for $j, k = s, n, z$. The results indicate that curved-flow turbulence is less efficient in producing shear than the straight-flow equivalent, with the same amount of turbulent kinetic energy. They show that this change in the turbulence structure is at the basis of the observed distributions of the turbulence properties. In the following, an analysis of the measured velocity fluctuations and the turbulence structure will be made that is complementary to that analysis and will confirm its results.

4. Analysis of velocity fluctuations and of turbulence structure

4.1. *Width-coherent velocity fluctuations*

As mentioned before, the ADVP has the advantage of measuring simultaneous profiles of the instantaneous velocity components along an entire line (instead of a single point). This line-by-line approach offers the possibility to investigate coherent structures along those lines. In the experiment (see figure 1), profiles extending over half the channel width are measured at different vertical levels. They enable us to investigate the time-behaviour of the system of circulation cells. The time-stack plot in figure 5 shows the transversal velocity fluctuations for the profiles at 3.4 cm and 9.3 cm below the water surface, i.e. at the level of the eye of the outer-bank cell and the core of minimum turbulent kinetic energy, respectively (cf. figures 3*b* and 4*b*). The streaks in this figure indicate that the transversal fluctuations are coherent over the width.

In order to quantify the coherence of these fluctuations, two-point correlations are evaluated via

$$R_{jj}(-7.5, n; z) = \frac{\overline{v_j'(n=-7.5, z)v_j'(n, z)}}{\sqrt{\overline{v_j'^2(n=-7.5, z)}}\sqrt{\overline{v_j'^2(n, z)}}}. \tag{3}$$

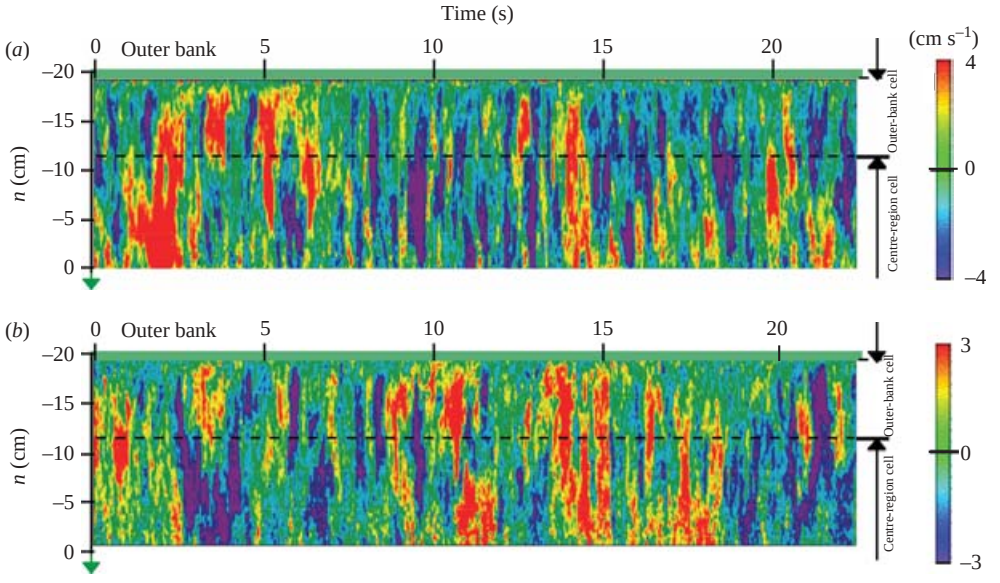

FIGURE 5. Time-series of transversal velocity fluctuations for profiles at (*a*) 3.4 cm and (*b*) 9.3 cm below water surface.

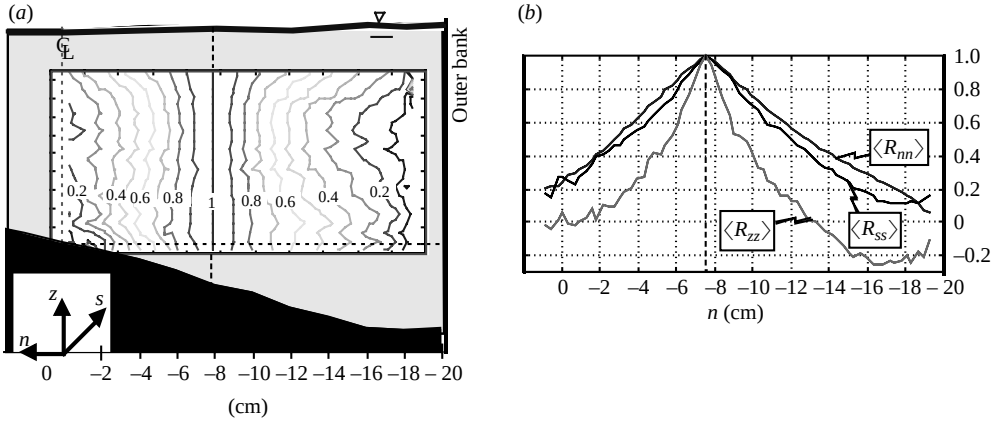

FIGURE 6. (*a*) Two-point correlation R_{nn} $(-7.5, n; z)$ between the transversal velocity fluctuations measured at 12.5 cm from the outer bank and points on the same transversal profile; (*b*) Vertically-averaged two-point correlations, $\langle R_{jj}\rangle (j = s,\ n,\ z)$.

The reference point of this correlation is arbitrarily located at $n = -7.5$ cm, i.e. at 12.5 cm from the outer bank. The correlation R_{nn} is shown in figure 6(*a*). As the results are similar throughout the water column, the vertical mean is representative of the entire vertical. Figure 6(*b*) shows the cross-stream distribution of these vertically averaged values, $\langle R_{jj}(-7.5, n)\rangle$.

Typical two-point correlations of homogeneous turbulence would show an initial steep descent around the reference point, down to values of about 1/3, followed by a tail with $R_{jj} < 1/3$ (Prandtl, Oswatitsch & Wieghardt 1990; Bruns, Fernholz & Monkewitz 1999). $\langle R_{zz}\rangle$ in figure 6(*b*) more or less follows this pattern, but $\langle R_{ss}\rangle$ and $\langle R_{nn}\rangle$ have a triangular shape and do not show any initial steep descent. This indicates that the downstream and transversal fluctuations are atypically coherent

over the width. In the outer-bank region, $\langle R_{zz} \rangle$ is negative, which indicates that the vertical fluctuations of the outer-bank cell are out of phase with those of the centre-region cell. This phenomenon, however interesting, will not be investigated in further detail. We will focus on the downstream and the transversal fluctuations.

4.2. *Decomposition of the velocity fluctuations*

Following Hussain (1983), the velocity fluctuations, v'_j, can be decomposed into slow and rapid fluctuations. Anticipating the results, we denote the slow fluctuations with the subscript w (wave) and the rapid ones with the subscript b (background turbulence):

$$v'_j(n, z, t) = v'_{j,w}(n, z, t) + v'_{j,b}(n, z, t) \qquad (j = s, n). \tag{4}$$

Hussain (1983) and Tamburrino & Gulliver (1999) made the split by taking a moving average over a time period long enough to eliminate the fast fluctuations, but short enough not to lose essential information on the slow fluctuations. We exploit the profiling capacity of the ADVP and make use of the observed width-coherence of the downstream and transversal velocity fluctuations (figure 6): we assume that the fast fluctuations are not coherent over the width, while the slow ones are. Therefore, we average the velocity fluctuations over the width range from $n = -14.7$ cm to $n = 0.9$ cm, i.e. over 53 measuring points (a region of 5.3 cm wide adjacent to the outer bank is omitted, because its transversal fluctuations may be geometrically hindered by the outer bank):

$$\{v'_{j,b}\}(z, t) \approx 0 \ll \{v'_{j,w}\}(z, t) \approx v'_{j,w}(n, z, t), \tag{5}$$

in which $\{\cdot\}$ denotes the width-averaging operation. Together with (4), this leads to:

$$v'_{j,w}(n, z, t) \approx \{v'_{j,w}\}(z, t) \approx \{v'_j\}(z, t), \tag{6}$$

whence

$$v'_j(n, z, t) = \{v'_j\}(z, t) + v'_{j,b}(n, z, t). \tag{7}$$

This provides an easily applicable method for first-order decomposition of the velocity fluctuations.

4.3. *Bulk-oscillation of the pattern of circulation cells*

We assume that the slow width-coherent fluctuations represent a bulk-oscillation of the pattern of circulation cells with migration speed $\boldsymbol{V}_{osc}(t) = (V_{s,osc}, V_{n,osc})(t)$. In the following, some experimental observations are presented that are in agreement with this assumption.

In an Eulerian framework, a rigid transverse displacement of the pattern of circulation cells over a distance $\Delta n(t) = \int V_{n,osc}\, \mathrm{d}t$ replaces the fluid particle at position n by the particle that originates from position $n - \Delta n(t)$, thus generating the slow Eulerian velocity variation:

$$\boldsymbol{v}^*(n, z, t) = \boldsymbol{v}(n - \Delta n(t), z) - \boldsymbol{v}(n, z). \tag{8}$$

An illustration for v_n^* is given in figure 7. Similar variations induced by the downstream migration, $\Delta s(t) = \int V_{s,osc}\, \mathrm{d}t$, are assumed to be small, since the downstream velocity gradients are presumably much smaller than the transversal ones, $\partial \boldsymbol{v}/\partial s \ll \partial \boldsymbol{v}/\partial n$; they are ignored for lack of information (measurements taken in one cross-section only).

The slow velocity variations corresponding to this bulk-oscillation can be written as:

$$\boldsymbol{v}'_w(n, z, t) = \boldsymbol{v}^*(n, z, t) + \boldsymbol{V}_{osc}(t). \tag{9}$$

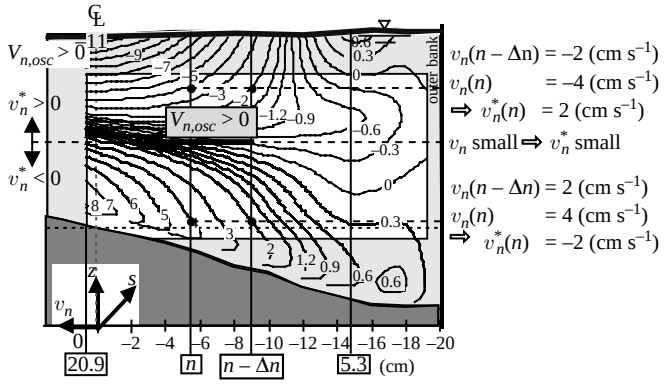

FIGURE 7. Isolines of transversal velocity, v_n(cm s^{-1}), to illustrate how a bulk transversal displacement Δn of the entire pattern leads to variations of the Eulerian transversal velocity.

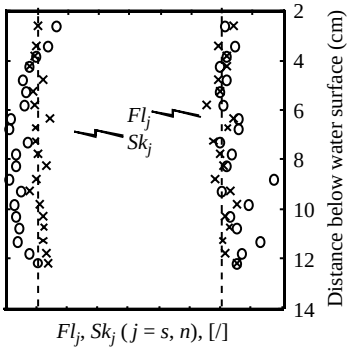

FIGURE 8. Skewness, Sk_j, and kurtosis, Fl_j, of the slow width-coherent fluctuations $\{v_j'\}$ $(j = s, n)$. ×, $\{v_s'\}$; ○, $\{v_n'\}$.

Combining (6) and (9) gives:

$$\{\boldsymbol{v}'\}(z,t) \approx \{\boldsymbol{v}^*\}(z,t) + \boldsymbol{V}_{osc}(t). \tag{10}$$

At about mid-depth, v_n and its radial derivative are small (figure 7). Accordingly, v_n^* is also small, whence $\{v_n'\} \approx V_{n,osc}$. In the upper part of the water column, v_n^* and $V_{n,osc}$ have the same sign, whereas they are of opposite sign in the lower part (see figure 7). Thus, if a bulk-oscillation of the pattern of circulation cells exists, $\{v_n'\}$ must have the following property:

$$\overline{\{v_n'\}^2} > \overline{V_{n,osc}^2} \qquad \text{in the upper part of the water column,} \tag{11}$$

$$\overline{\{v_n'\}^2} \approx \overline{V_{n,osc}^2} \qquad \text{at about mid-depth,} \tag{12}$$

$$\overline{\{v_n'\}^2} < \overline{V_{n,osc}^2} \qquad \text{in the lower part of the water column.} \tag{13}$$

In the next section, we will show that the measured profile of $\overline{\{v_n'\}^2}/u_{*,60}^2$ has this property.

As $\{v_n^*\}(z,t)$, and thus $\{v_n'\}(z,t)$, are mainly generated by the transversal component of the bulk-oscillation, they should have the same symmetry properties as $V_{n,osc}(t)$. Figure 8 shows that both the skewness $Sk_n = \overline{\{v_n'\}^3}/(\overline{\{v_n'\}^2})^{3/2}$ and the kurtosis (also called flatness) $Fl_n = \overline{\{v_n'\}^4}/(\overline{\{v_n'\}^2})^2$ are rather uniform over the depth, as they are by definition for $V_{n,osc}(t)$. The figure also shows that the skewness of $\{v_n'\}$ is rather

small ($Sk_n < -0.5$), which indicates that the width-coherent transversal fluctuations are rather symmetrical in time. The kurtosis is nearly constant at $Fl_n = 3$, which corresponds to the value for a Gaussian process. Figure 8 also shows the skewness and the kurtosis of the width-coherent downstream oscillations $\{v_s'\}$. The skewness is nearly constant at $Sk_s \approx 0$, indicating symmetrical fluctuations, and the kurtosis is nearly constant at $Fl_s = 3$.

This all adds up to the suggestion that a bulk-oscillation exists. In the next sections, we will further investigate the properties of that oscillation and the remaining turbulence.

4.4. *Decomposition of the turbulent stresses*

The kinetic energy content of the width-coherent fluctuations and the background-turbulence is analysed by decomposing the Reynolds normal stresses in a similar way as the turbulent fluctuations (cf. equation (7)):

$$\overline{v_j'^2}(n, z) = \overline{\{v_j'\}^2}(z) + \overline{v_{j,b}'^2}(n, z) + 2\overline{\{v_j'\}v_{j,b}'}(n, z) \qquad (j = s, n). \tag{14a}$$

Figure 9 shows the results:

(i) the normal stresses due to the total velocity fluctuations, $\overline{v_j'^2}$ (figure 9*a*, *b*);

(ii) the normal stress contributions due to the background turbulence, $\overline{v_{j,b}'^2}$ (figure 9*c*, *d*); both the downstream and the normal component are high in the outer-bank shear layer, decrease to a minimum near the edge of the outer-bank region, and then increase towards the inner bend;

(iii) the normal stress contributions due to the width-coherent fluctuations, $\overline{\{v_j'\}^2}$ (figure 9*e*), which are of the same order of magnitude as those due to the background turbulence.

Note that the contribution due to the interaction between the background turbulence and the width-coherent fluctuations, $2\overline{\{v_j'\}v_{j,b}'}(n, z)$ (to be evaluated from 14(*a*) and figure 9), is not negligible and takes positive as well as negative values on the measuring grid. For further details on the distributions of the total normal stress components $\overline{v_j'^2}$, we refer to Blanckaert & Graf (2001).

As stated before (equation (12)), the normal stress contribution due to the transversal bulk-oscillation $V_{n,osc}(t)$ at about mid-depth can be approximated by $\sqrt{\overline{V_{n,osc}^2}}/u_{*,60} \approx \sqrt{\overline{\{v_n'\}^2}}/u_{*,60} \approx 0.4$ (figure 9*e*), i.e. $\sqrt{\overline{V_{n,osc}^2}} \approx \sqrt{\overline{\{v_n'\}^2}} \approx 0.02\,\mathrm{m\,s^{-1}}$. Figure 9(*e*) shows that the downstream component of the width-coherent fluctuations is considerably larger than the transversal one: $\sqrt{\overline{\{v_s'\}^2}}/u_{*,60} \approx 0.6$. This high value suggests that $\overline{\{v_s'\}^2}$ is not primarily induced by the transversal displacement of the pattern of circulation cells, but that the bulk-oscillation has an important downstream component, $V_{s,osc}(t)$. More extensive measurements, simultaneously covering more than one cross-section, will be needed to investigate this.

The shear stress $\overline{v_s'v_n'}$ is decomposed in line with (7):

$$\overline{v_s'v_n'}(n, z) = \overline{\{v_s'\}\{v_n'\}}(z) + \overline{v_{s,b}'v_{n,b}'}(n, z) + \overline{\{v_s'\}v_{n,b}'}(n, z) + \overline{v_{s,b}'\{v_n'\}}(n, z). \tag{14b}$$

Figure 10(*a*) shows the normalized total shear stress $-\overline{v_s'v_n'}/u_{*,60}^2$, figure 10(*b*) the normalized shear stress, $-\overline{\{v_s'\}\{v_n'\}}|_{f<3[Hz]}/u_{*,60}^2$, generated by the width-coherent velocity fluctuations. In the latter, the high-frequency contributions for $f > 3\,\mathrm{Hz}$ have been filtered out, because they are considered to be parasitic (see figures 11*a* and 12*b*). Comparison with the normalized total shear stress shows that the width-coherent fluctuations have a relatively small contribution to the shear stress.

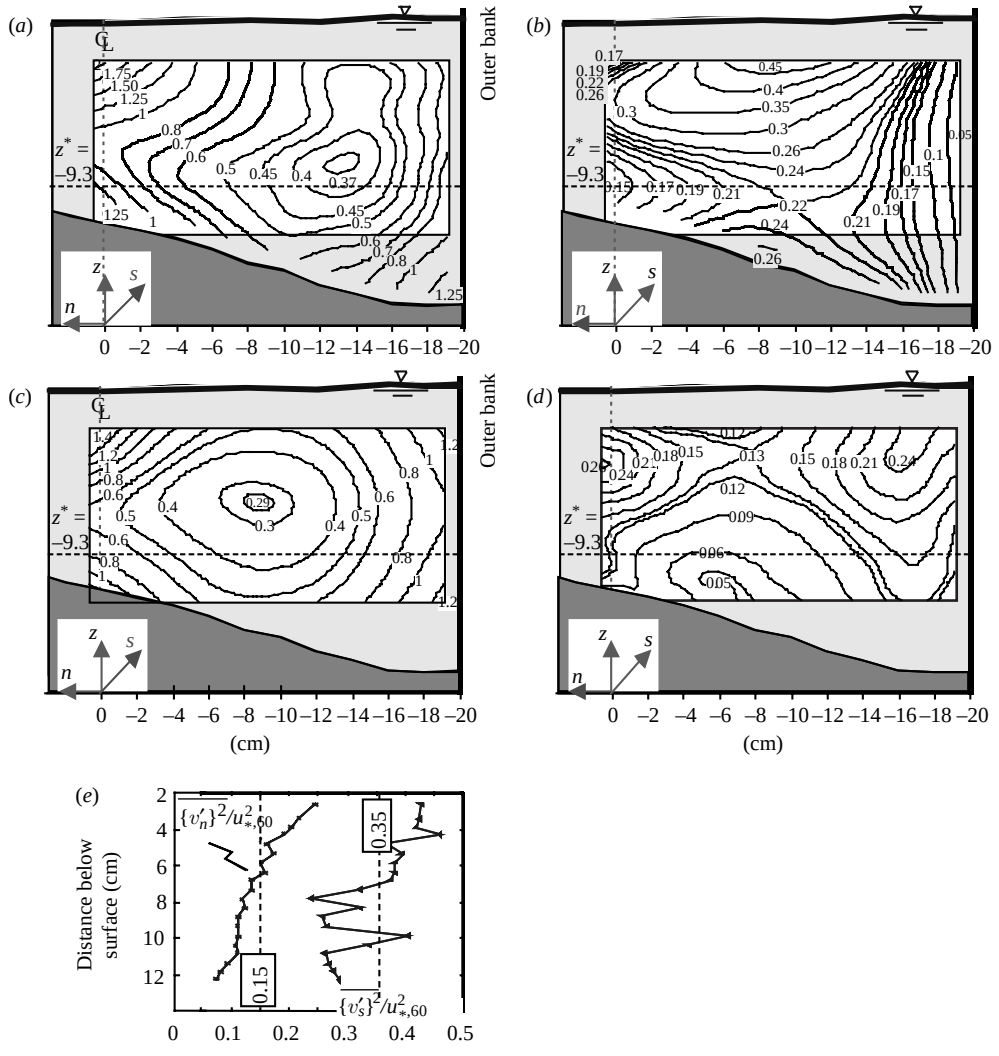

FIGURE 9. Turbulent normal stresses (*a*) $\overline{v_s'^2}$ and (*b*) $\overline{v_n'^2}$; contributions to normal stresses by background turbulence (*c*) $\overline{v_{s,b}'^2}$ and (*d*) $\overline{v_{n,b}'^2}$; and (*e*) by width-coherent flucuations $\overline{\{v_s'\}^2}$ and $\overline{\{v_n'\}^2}$. All normalized by $u_{*,60}^2$.

In summary, when treated as turbulence, the width-coherent fluctuations contribute significantly to the normal stresses, but much less to the shear stress. Velocity fluctuations that do not generate shear are not representative of developed turbulence, but rather indicate a wavelike motion. This will be further investigated in the following by means of a spectral analysis of the velocity fluctuations.

4.5. *Spectral analysis of the structure of turbulence*

A spectral analysis of the width-coherent fluctuations $\{v_j'\}$ and of the background turbulence $v_{j,b}'$ is performed to investigate their structure. In line with the way the experimental data have been processed, the fluctuating signals are decomposed into Fourier components, as:

$$x_j'(t) = \sum_{\alpha=1}^{N} a_{j,\alpha} \cos(2\pi t f_\alpha + \phi_{j,\alpha}) \qquad (j = s, n), \tag{15}$$

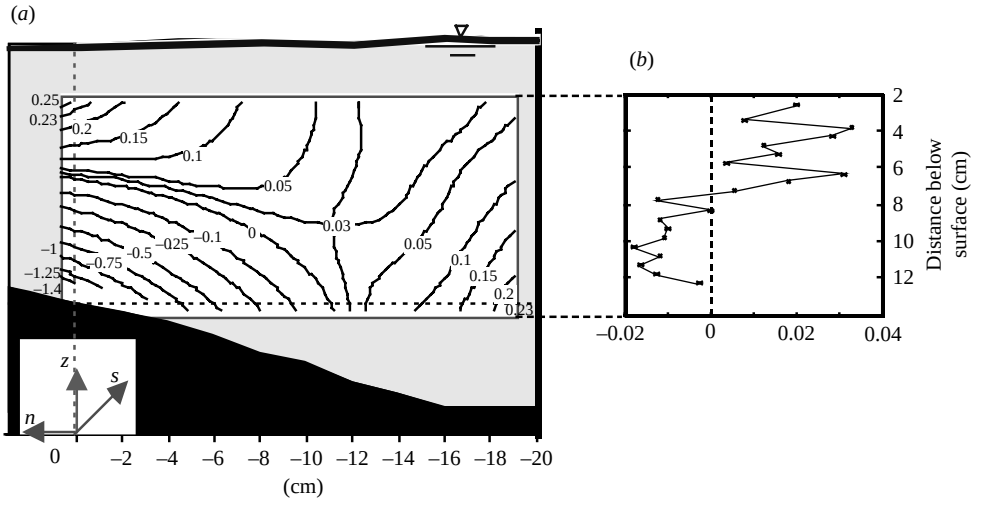

FIGURE 10. Normalized shear stress generated by: (*a*) total velocity fluctuations, $-\overline{v_s' v_n'}/u_{*,60}^2$; (*b*) width-coherent velocity fluctuations, $-\overline{\{v_s'\}\{v_n'\}}|_{f<3\,(\mathrm{HZ})}/u_{*,60}^2$.

in which x_j' stands for $\{v_j'\}$ or $v_{j,b}'$, $a_{j,\alpha}$ and $\phi_{j,\alpha}$ are the amplitude and phase of the component with frequency $f_\alpha = \alpha f_1$, f_1 is the basic frequency and f_N is the Nyquist frequency, i.e. half the sampling frequency.

The power spectral density function, $F(f)$, and its cumulative equivalent, $\Im(f)$, indicate the contribution of each frequency range to the intensity of the fluctuating signal:

$$\Im(f) = \overline{x'^2}(\hat{f} < f) = \int_0^f F(\hat{f})\,\mathrm{d}\hat{f}. \tag{16}$$

These continuous functions of f are approximated by their discrete Fourier-series counterpart (for simplicity, the same notations have been used for the continuous functions and the discrete approximations):

$$\Im(f_m) = \overline{x'^2}(f < f_m) = \sum_{\alpha=1}^{m} F(f_\alpha)(f_\alpha - f_{\alpha-1}) \qquad (m = 1, \ldots, N). \tag{17}$$

Equation (16) can also be written as:

$$\Im(f_m) = \int_0^f F(\hat{f})\,\mathrm{d}\hat{f} = \int_0^f \hat{f} F(\hat{f})\,\mathrm{d}(\ln \hat{f}) \qquad (m = 1, \ldots, N) \tag{18}$$

indicating that in a graphical representation with a logarithmic frequency scale, the contribution of each frequency range is visualized by the area under the graph of $fF(f)$, or $f_\alpha F(f_\alpha)$ ($\alpha = 1, \ldots, N$) for the discrete approximation.

Similar F-functions (spectra) of the width-coherent fluctuations were found at each measured elevation. Therefore, and to reduce scatter, only the vertical mean, $f\langle F\rangle$, is shown in figure 11(*a*). The main contribution to $\overline{\{v_s'\}^2}$ lies in the frequency range $f < 1$ Hz, with a maximum around $f = 0.1$ Hz, whereas the main contribution to $\overline{\{v_n'\}^2}$ is found in the range $f = 0.3$–2 Hz. This indicates that the pattern of circulation cells does not oscillate with a characteristic dominant frequency, but rather in a range of low frequencies, 0.1 Hz $< f <$ 2 Hz. The F-functions of $\{v_s'\}$ and $\{v_n'\}$ both contain a

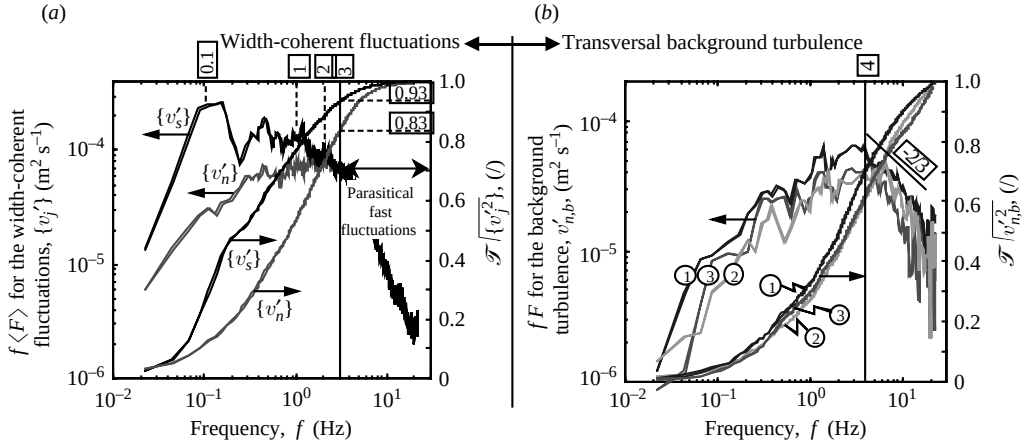

FIGURE 11. (*a*) Frequency × power spectral density, $f\langle F\rangle$, and normalized cumulative power spectral density, $\langle\mathfrak{I}\rangle/\{v_j'\}^2$, for width-coherent fluctuations, $\{v_s'\}$ and $\{v_n'\}$, averaged over all measured profiles; (*b*) frequency × power spectral density, fF and normalized power spectral density, $\mathfrak{I}/\overline{v_{n,b}'^2}$, for transversal background turbulence, $v_{n,b}'$, in three points with coordinates (1) $(n, z^*) = (-12, -9.3)$; (2) $(-7.5, -9.3)$; (3) $(-3, -9.3)$.

high-frequency tail which does not refer to a low-frequency width-coherent motion. Based on our results (further see figure 12*b*), we assume that frequencies above 3 Hz are parasitical. The $\mathfrak{I}$-function shows that this parasitical tail represents less than 10 % of $\overline{\{v_s'\}^2}$ and less than 20 % of $\overline{\{v_n'\}^2}$. This does not alter our previous conclusion that the width-coherent fluctuations contribute significantly to the turbulent normal stresses.

Figure 11*b* also shows the F- and $\mathfrak{I}$-functions of the background-turbulence fluctuations $v_{n,b}'$ in the points at $n = -12$, -7.5 and -3 cm, respectively, at 9.3 cm below the water surface. These points are chosen in regions with low and high levels of background-turbulence (see figure 9*c*, *d*). The maximum contributions to the background-turbulence are found around $f = 4$ Hz. Figure 11 also shows an inertial subrange – corresponding to a slope of –2/3 (–5/3 in a log-log $F(f)$-plot). The observed F- and $\mathfrak{I}$-functions of the background-turbulence fluctuations have a form typical of developed turbulence. Similar F- and $\mathfrak{I}$-functions were found for the downstream background-turbulence fluctuations, $v_{s,b}'$. These F- and $\mathfrak{I}$-functions indicate that the width-coherent fluctuations and the background turbulence have different spectral characteristics.

It was shown in the foregoing that the width-coherent fluctuations significantly contribute to the normal stresses, but generate little shear stress. The efficiency with which fluctuating velocities generate turbulent shear stresses, given the kinetic energy of the velocity fluctuations, is an important characteristic of the turbulence structure. In the following, it will be analysed by computing the turbulent shear stresses and the turbulent normal stresses from the Fourier-series representations of the fluctuating velocities, as:

$$\overline{x_j' x_k'} = \frac{1}{T_s}\int_0^T \left[\sum_{\alpha=1}^{N} a_{j,\alpha}\cos(2\pi t f_\alpha + \phi_{j,\alpha})\right]\left[\sum_{\beta=1}^{N} a_{k,\beta}\cos(2\pi t f_\beta + \phi_{k,\beta})\right] \mathrm{d}t \quad (j,k = s,n), \quad (19)$$

in which T_s is the sampling time. Using the orthogonality characteristic of the Fourier components,

$$\frac{1}{T_s}\int_0^T \cos(2\pi t f_\alpha + \phi_{s,\alpha})\cos(2\pi t f_\beta + \phi_{n,\beta})\,\mathrm{d}t = \tfrac{1}{2}\cos(\phi_{n,\beta} - \phi_{s,\alpha})\delta_{\alpha\beta} \tag{20}$$

which is valid for long sampling periods, $T_s \gg 1/f_\alpha, 1/f_\beta$, the shear stresses and the normal stresses can be expressed as:

$$\overline{x'_s x'_n} = \tfrac{1}{2}\sum_{\alpha=1}^{N} a_{s,\alpha} a_{n,\alpha}\cos(\phi_{n,\alpha} - \phi_{s,\alpha}), \tag{21}$$

$$\overline{x'^2_j} = \tfrac{1}{2}\sum_{\alpha=1}^{N} a^2_{j,\alpha} \qquad (j = s, n). \tag{22}$$

The efficiency by which the turbulent fluctuations at frequency f_α generate shear stresses can be quantified by the ratio,

$$\frac{\overline{x'_s x'_n}^2}{\overline{x'^2_s}\;\overline{x'^2_n}}(f_\alpha) = \cos^2(\phi_{n,\alpha} - \phi_{s,\alpha}), \tag{23}$$

which means that it depends only on the phase lag, $\phi_{n,\alpha} - \phi_{s,\alpha}$. These phase lags enable us to distinguish between developed turbulence and wavelike motion (McBeans & Miyake 1972; Komori *et al.* 1983). The efficiency of shear stress generation is high for developed turbulence, with phase lags typically around i π (i $= -1, 0, 1$), whereas wavelike velocity fluctuations hardly generate shear stresses and have phase lags typically around $\pm\pi/2$.

As shown before, the width-coherent velocity fluctuations $\{v'_s\}$ and $\{v'_n\}$ are inefficient in generating shear stress. Figure 12(*a*) shows the phase lags at each frequency between the components of $\{v'_s\}$ and $\{v'_n\}$ for the profile at 9.3 cm below the water surface. For $f < 1.5$ Hz, these phase lags are largely scattered around values of $\phi_{n,\alpha} - \phi_{s,\alpha} \approx \pi/2$. Because of the large scatter in this figure, the same data are presented in an alternative way. The phase lags for the width-coherent fluctuations have been calculated at each measured elevation, and those for the background turbulence have been calculated in each measured point. For each frequency, f_α, the percentage of all phase lags found around $\pm\pi/2$ ($0.3\pi \leqslant \|\phi_{n,\alpha} - \phi_{s,\alpha}\| \leqslant 0.7\pi$) and around $\pm i\pi$ ($\|\phi_{n,\alpha} - \phi_{s,\alpha}\| \leqslant 0.2\pi$ or $0.8\pi \leqslant \|\phi_{n,\alpha} - \phi_{s,\alpha}\|$) is shown in figures 12(*b*) and 12(*c*) for the width-coherent fluctuations and the background turbulence, respectively. The phase lags of the width-coherent fluctuations (figure 12*b*) show a different behaviour in the low- and high-frequency ranges, separated at about 1.5 Hz. In the low-frequency range, at least in the range that contributes most to the width-coherent normal stresses ($f \approx 0.4 \div 1$ Hz; figure 11*a*), they are mainly found around $\pm\pi/2$. In the high-frequency range they occur mainly around 0 and $\pm\pi$. It is on the basis of this result that we have chosen to consider the contributions with $f > 3$ Hz as fast parasitical fluctuations. The phase lags of the background-turbulence fluctuations (figure 12*c*) are mainly found around 0 and $\pm\pi$ in the low-frequency range and tend to be more randomly distributed at higher frequencies.

Thus, the decomposition of the velocity fluctuations into width-coherent fluctuations and background turbulence seems to be physically meaningful, since they have a fundamentally different turbulence structure. The width-coherent fluctuations seem to represent a bulk-oscillation of the pattern of circulation cells with the characteristics of a wavelike motion, i.e. with a low efficiency in shear generation.

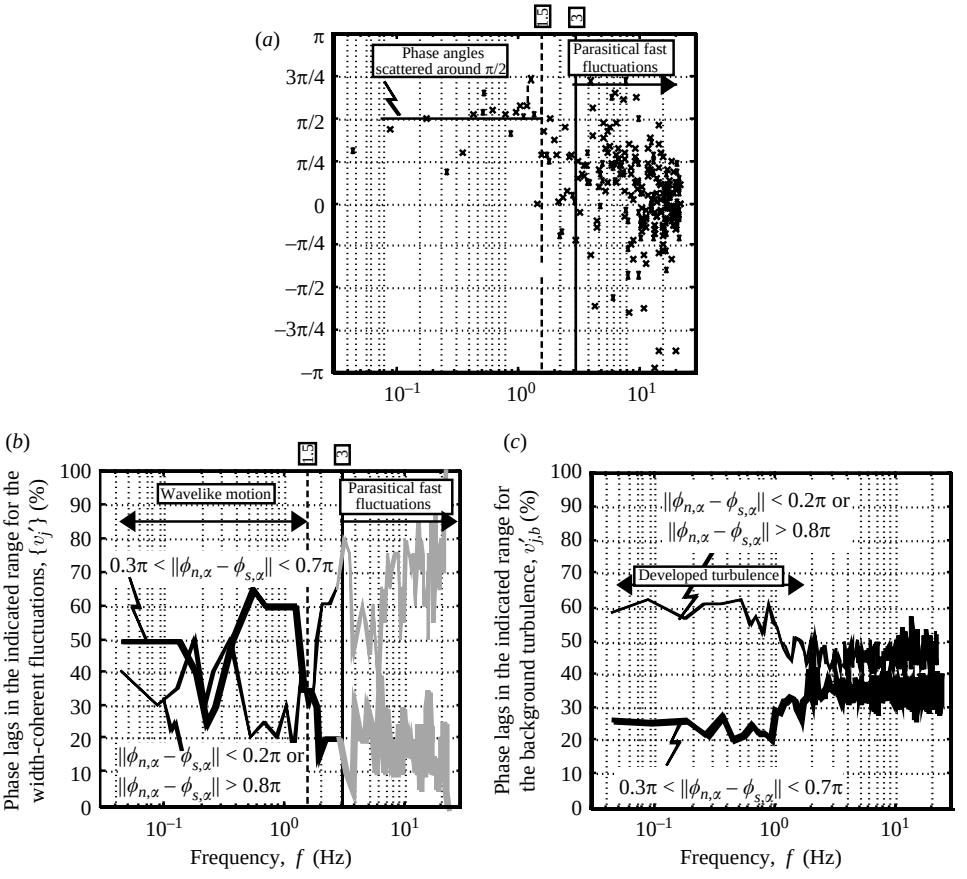

FIGURE 12. Phase lags $\phi_{n,\alpha} - \phi_{s,\alpha}$ between (*a*) width-coherent fluctuations $\{v'_s\}$ and $\{v'_n\}$ for profile at 9.3 cm below water surface; (*b*) width-coherent fluctuations $\{v'_s\}$ and $\{v'_n\}$ averaged over measuring grid; (*c*) background-turbulence fluctuations $v'_{s,b}$ and $v'_{n,b}$ averaged over measuring grid.

The background turbulence has the characteristics of developed turbulence and is much more efficient in shear generation. All departures from the turbulence structure in straight uniform shear flow are directly or indirectly due to the streamline curvature of the mean flow. Blanckaert & de Vriend (2005) have shown that the departures of the measured turbulence structure from its counterpart in straight uniform shear flow seem to be related to a curvature-flux-Richardson number R_f that reflects the streamline curvature. The relation between the experimentally observed turbulence characteristics and the streamline curvature will be further elaborated in the next section.

5. The influence of streamline curvature

Bradshaw (1969, 1973) has shown, for two-dimensional flows that are curved in their own plane, that the structure of turbulence is sensitive to streamline curvature and stipulated that the influence of streamline curvature is analogous to the influence of buoyancy in a density-stratified flow. The analysis that is generally used to derive buoyancy parameters from the equations of motion can be used to derive equivalent

parameters for streamline curvature. In the present case of three-dimensional flow, curved in the horizontal plane, such parameters can be defined as:

$$\omega_{BV} = \sqrt{2\frac{v_s}{r_{sn}^2}\frac{\partial r_{sn} v_s}{\partial n}} \qquad [\mathrm{Hz}], \tag{24}$$

$$S = \frac{v_s}{r_{sn}} \Big/ \frac{\partial v_s}{\partial n}, \tag{25}$$

$$Ri = 2\frac{v_s}{r_{sn}^2}\frac{\partial r_{sn} v_s}{\partial n} \Big/ \left(\frac{\partial v_s}{\partial n}\right) = 2S(1+S), \tag{26}$$

$$R_f = \frac{2\overline{v_s' v_n'}\dfrac{v_s}{r_{sn}}}{\overline{v_s' v_n'}\dfrac{1}{r_{sn}}\dfrac{\partial r_{sn} v_s}{\partial n}} = \frac{2\dfrac{v_s}{r_{sn}}}{\dfrac{1}{r_{sn}}\dfrac{\partial r_{sn} v_s}{\partial n}} = \frac{2S}{1+S}, \tag{27}$$

in which v_s represents the velocity along the streamline and r_{sn} the radius of curvature of the streamline in the (s, n)-plane. The latter can be evaluated from the experimental data using:

$$\frac{1}{r_{sn}} = \frac{1}{r'_{sn}} + \frac{1}{1+n/r}\frac{1}{R}, \tag{28}$$

R being the centreline curvature, and

$$\begin{aligned}\frac{1}{r'_{sn}} &\approx \frac{\mathrm{d}^2 n}{\mathrm{d}s^2} = \frac{\mathrm{d}}{\mathrm{d}s}\left(\frac{v_n}{v_s}\right) = \frac{1}{v_s^2}\left(v_s\frac{\mathrm{d}v_n}{\mathrm{d}s} - v_n\frac{\mathrm{d}v_s}{\mathrm{d}s}\right)\\ &\approx \frac{1}{v_s^2}\left[\left(v_n\frac{\partial v_n}{\partial n} + v_z\frac{\partial v_n}{\partial z}\right) - \frac{v_n}{v_s}\left(v_n\frac{\partial v_s}{\partial n} + v_z\frac{\partial v_s}{\partial z}\right)\right],\end{aligned} \tag{29}$$

based on

$$\frac{\mathrm{d}v_i}{\mathrm{d}s} = \frac{\partial v_i}{\partial s} + \frac{\partial v_i}{\partial n}\frac{v_n}{v_s} + \frac{\partial v_i}{\partial z}\frac{v_z}{v_s} \quad (i = s,\ n) \tag{30}$$

and the assumption $\frac{\partial v_i}{\partial s} \approx 0$.

Clearly, this derivation is restricted to plane curved flows.

The frequency ω_{BV} was first derived by von Kármán (1934) from a simple linear stability analysis. He showed that when an element of fluid is transversally displaced in a plane frictionless curved (or rotating) flow, it will either move further away from its original position or return towards it and oscillate about it. If ω_{BV} is real, it represents the frequency of this oscillation. An imaginary ω_{BV} indicates exponential growth or decay. The frequency ω_{BV} is similar to the Brünt–Väisälä frequency in density-stratified flow.

The dimensionless curvature parameter S (equation (25)) derived by Prandtl (1930) represents the ratio of the curvature-induced extra strain-rate to the inherent strain-rate. When dividing the square of ω_{BV} by $(\partial v_s/\partial n)^2$, which is a typical frequency scale of a shear flow, we obtain the curvature-gradient-Richardson number Ri (equation (26)). Whilst ω_{BV}, S and Ri are related to static stability and do not involve turbulence, the curvature-flux-Richardson number R_f (equation (27)) is derived from the Reynolds stress equations. It is interpreted as minus the ratio of the curvature-induced $\overline{v_n'^2}$-production to the total $\overline{v_s'^2}$-production. It is positive/negative for stabilizing/destabilizing curvature. According to (24)–(27), S, Ri and R_f are

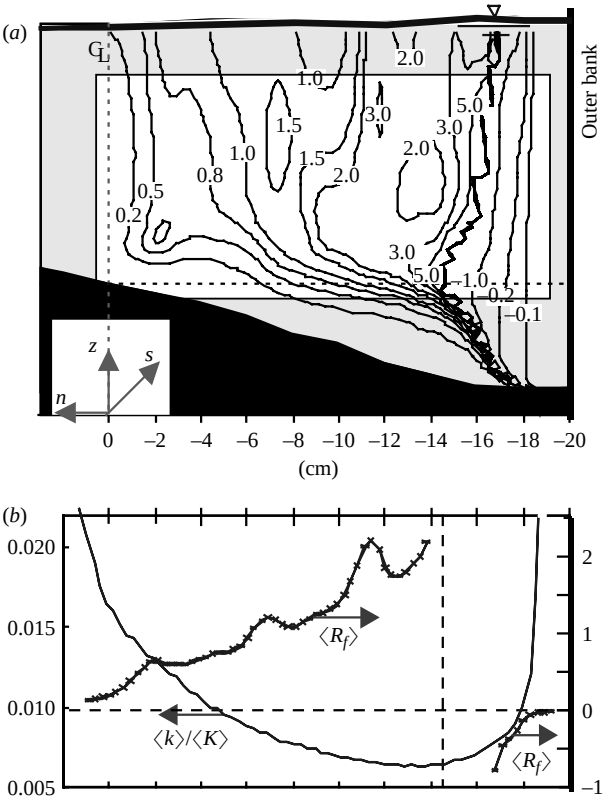

FIGURE 13. (*a*) Flux-curvature-Richardson number, R_f; (*b*) Depth-averaged flux-curvature-Richardson number, $\langle R_f \rangle$, and ratio, $\langle k \rangle / \langle K \rangle$ (copied from figure 4*c*).

closely related:

$$R_f = Ri/(1+S)^2 = 2S/(1+S) \quad \text{whence} \quad R_f \approx Ri \approx 2S \quad \text{for small } S. \tag{31}$$

Blanckaert & de Vriend (2005) show that in the present strongly three-dimensional flow, the reduction of turbulence activity in the deepest part of the cross-section seems to be related to the curvature-flux-Richardson number R_f. Their findings are briefly summarized here. Figure 13(*a*) shows the experimental distributions of R_f and figure 13(*b*) compares the distributions of its depth-averaged value $\langle R_f \rangle$ with that of $\langle k \rangle / \langle K \rangle$ (copied from figure 4*c*). In most of the area, R_f and $\langle R_f \rangle$ are positive and increase in outward direction from small values near the centreline to maximum values $O(2)$. In the outer-bank shear layer, where R_f and $\langle R_f \rangle$ are negative, the influence of the sidewall proximity dominates the influence of the streamline curvature.

There seems to be a strong negative relation between the distributions of $\langle R_f \rangle$ and $\langle k \rangle / \langle K \rangle$. Near the centreline, where $\langle R_f \rangle \sim 0$, $\langle k \rangle / \langle K \rangle$ approaches its straight-uniform-flow value of 0.03. The outward reduction of $\langle k \rangle / \langle K \rangle$ is accompanied by increasing values of $\langle R_f \rangle$, and the maximum of $\langle R_f \rangle$ coincides with the minimum of $\langle k \rangle / \langle K \rangle$. In the outer-bank shear layer, $\langle R_f \rangle < 0$ and $\langle k \rangle / \langle K \rangle$ strongly increases. As in two-dimensional flows, positive values of R_f in curved flow go with a reduction of the turbulent kinetic energy. Note that the extrapolations outside the measuring grid do not significantly alter these results.

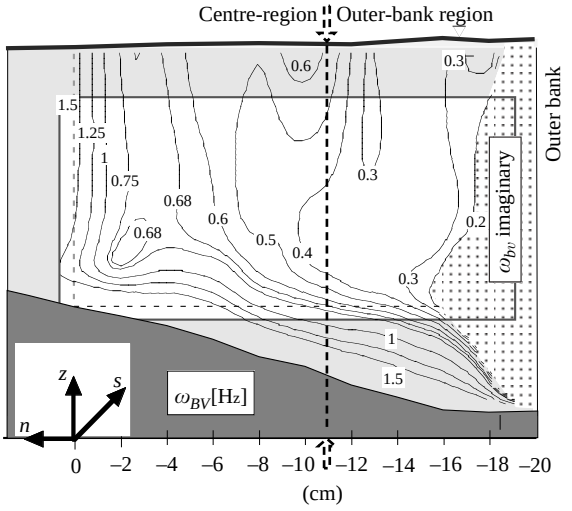

FIGURE 14. Theoretical frequency, ω_{bv} (Hz), of a transversally displaced fluid element.

Figure 14 shows the distribution of the frequency ω_{BV} (equation (24)). The calculated values are uniform over most of the flow depth, except close to the bed. Near the outer bank, where the curvature has a destabilizing effect, ω_{BV} is imaginary. Values of the order of 0.3 Hz are found in the region where the ratio $\langle k\rangle/\langle K\rangle$ is minimum. Near the centreline, where the ratio $\langle k\rangle/\langle K\rangle$ strongly increases, ω_{BV} goes up to values of about 1.5 Hz. These values of ω_{BV} are comparable to the observed dominant frequency ranges of the width-coherent wavelike velocity fluctuations $\{v_s'\}$ and $\{v_s'\}$ shown in figure 11(*a*).

Thus, both the bulk-oscillation of the pattern of circulation cells and the reduction of turbulence activity seem to be related to parameters representative of the streamline curvature. The derivation of the curvature parameters ω_{BV} and R_f is based on a linear analysis for small streamline curvatures in two-dimensional curved flow in the (s,n)-plane (Bradshaw 1969). Our experiment concerns highly three-dimensional strongly curved flow, with complicating factors such as a relatively strong cross-stream motion, the proximity of the banks and a non-trivial bed topography. It is remarkable that even in such a complicated flow, the reduction of turbulence and its tendency towards wavelike motion seem to be related to simple streamline-curvature parameters such as ω_{BV} and R_f. However, a larger amount of experimental data is needed to confirm these results.

Strong turbulence damping and the transformation of low-frequency turbulence to a wavelike motion have been reported in the literature for different configurations. So & Mellor (1973) investigated turbulent boundary layers along a convex surface of varying curvature in a wind tunnel. In a region of stabilizing curvature, $S \approx 0.3$, they measured small turbulent normal stresses and nearly zero shear stresses. They speculate that this represents linear internal waves. Irwin & Smith (1975) derived a model of streamline curvature effects from the simplified Reynolds stress equations, and tested it against experimental data from curved wall jets in still air. The model predicts that turbulence reduces to wavelike motion for $S \approx 0.1$. Holloway & Tavoularis (1992) and Chebbi, Holloway & Tavoularis (1998) experimented on the effects of curvature on sheared turbulence in a wind tunnel, relatively isolated from wall and entrainment effects. They found that turbulence approaches wavelike motion

for $S \approx 0.33$. Holloway & Tavoularis (1998) presented a geometric explanation for the effects of mild streamline curvature on the turbulence anisotropy. McBean & Miyake (1972) took measurements in density-stratified atmospheric boundary layers and found that the shear stress generation decreases with increasing stability and that internal waves appear. Komori *et al.* (1983) experimentally investigated stably density-stratified open-channel flow and found that turbulent motion approaches wavelike motion with increasing Richardson number, $Ri \approx 0.3$ to 1. Our observation of a reduced turbulence activity and a tendency to wavelike motion complies qualitatively with these observations.

6. Discussion and conclusions

Non-intrusive three-dimensional mean flow and turbulence measurements were made in the outer half of one cross-section of an open-channel bend, using an acoustic Doppler velocity profiler (ADVP), which enables tracing coherent flow structures.

The downstream mean velocity v_s increases towards the outer bend and the maximum velocities are found in the lower part of the water column. A bi-cellular pattern of cross-stream circulation exists: besides a centre-region cell (the classical helical motion), a weaker counter-rotating cell occurs near the water surface adjacent to the outer bank. The turbulence activity in most of the outer bend is rather strongly reduced, as compared with straight uniform shear flow.

The analysis presented herein gives more physical insight into the turbulence dynamics, which can speculatively be described as follows. Similar to the influence of buoyancy, streamline curvature can lead to turbulence damping. This phenomenon is characterized by parameters such as the curvature-flux-Richardson number R_f, or the Brünt–Väisälä frequency ω_{bv}. Whereas increasing Reynolds numbers favour the turbulence activity, increasing streamline curvatures seem to suppress it. This damping occurs basically through a change in the turbulence structure, which goes with a less effective shear production.

The velocity fluctuations are atypically coherent over the width. The velocity signal is therefore decomposed into width-coherent fluctuations and rapidly varying background turbulence. The coherent fluctuations seem to represent a bulk-oscillation of the pattern of circulation cells in the downstream and transversal directions, which is significant in magnitude, nearly symmetrical and Gaussian. When treated as turbulence, it contributes significantly to the turbulent normal stresses (and thus also to the turbulent kinetic energy), but little to the turbulent shear stresses. The structures of the width-coherent velocity fluctuations and of the background turbulence are fundamentally different. The former have the characteristics of a wavelike motion (linear internal waves), with little shear stress generation, whereas the latter has the characteristics of developed turbulence with the usual efficiency of the shear stress generation. As part of the velocity fluctuations are organized in a coherent wavelike motion, the efficiency of shear generation is less than in straight uniform flow with the same total kinetic energy of the velocity fluctuations.

These results are comparable to the reduced levels of turbulence activity and the tendency to wavelike motion reported in literature for the cases of curved wind tunnels and density-stratified flows. The suppression of turbulence activity, in favour of a coherent wavelike motion, is an important phenomenon in curved open-channel flows, as it will affect the mixing and transport capacity of the flow and the forces exerted on the flow boundaries.

The experimental research is at present being extended by measuring in different sections all around the bend and under various hydraulic conditions.

This research was sponsored by the Swiss National Science Foundation under grants 2100-052257.97/1 and 2000-059392.99/2. K. B. acknowledges his PhD supervisor W. H. Graf, as well as Professor Zech and Professor Booij for their reviews of the paper. The reviewers are acknowledged for their constructive comments.

REFERENCES

Blanckaert, K. 2002 Flow and turbulence in sharp open-channel bends. PhD-thesis 2545, Ecole Polytechnique Fédérale Lausanne, Switzerland. (also available at ftp://lrhmac15.epfl.ch/Pub/Thesis/Blanckaert).

Blanckaert, K. & Graf, W. H. 2001 Experiments on flow in an open-channel bend. Mean flow and turbulence. *J. Hydraul. Engng ASCE*, **127**, 835–847.

Blanckaert, K. & Graf, W. H. 2004 Momentum transport in sharp open-channel bends. *J. Hydraul. Engng ASCE*, **130**, 186–198.

Blanckaert, K. & Lemmin, U. 2005 Means of noise reduction in acoustic turbulence measurements. *J. Hydraul. Res.* (in press).

Blanckaert, K. & de Vriend, H. J. 2003 Non-linear modeling of mean flow redistribution in curved open channels. *Water Resources Res.* **39**, 1375.

Blanckaert, K. & de Vriend, H. J. 2004 Secondary flow in sharp open-channel bends. *J. Fluid Mech.* **498**, 353–380.

Blanckaert, K. & de Vriend 2005 Turbulence characteristics in sharp open-channel bends. *Phys. Fluids* **17**, 055102.

Bradshaw, P. 1969 The analogy between streamline curvature and buoyancy in turbulent shear flow. *J. Fluid Mech.* **36**, 177–191.

Bradshaw, P. 1973 Effects of streamline curvature on turbulent flow. *AGARDograph* 169, NATO.

Bruns, J. M., Fernholz, H. H. & Monkewitz, P. A. 1999 An experimental investigation of a three-dimensional turbulent boundary layer in an S-shaped duct. *J. Fluid Mech.* **393**, 175–213.

Chebbi, B., Holloway, A. G. L. & Tavoularis, S. 1998 The response of sheared turbulence to changes in curvature. *J. Fluid Mech.* **358**, 223–244.

Dietrich, W. E. 1987 Mechanics of flow and sediment transport in river bends. In *River channels: Environment and Process* (ed. K. Richards), p. 391. Inst. Brit. Geogr. spec. publ. Oxford.

Holloway, A. G. L. & Tavoularis, S. 1992 The effects of curvature on sheared turbulence. *J. Fluid Mech.* **237**, 569–603.

Holloway, A. G. L. & Tavoularis, S. 1998 Geometric explanation of the effects of mild streamline curvature on the turbulence anisotropy. *Phys. Fluids* **10**, 1733–1741.

Hurther, D. 2001 3-D acoustic Doppler velocimetry and turbulence in open-channel flow. PhD thesis 2395, Ecole Polytechnique Fédérale Lausanne, Switzerland.

Hurther, D. & Lemmin, U. 1998 A constant beamwidth transducer for three-dimensional Doppler profile measurements in open channel flow. *Meas. Sci. Technol.* **9**, 1706–1714.

Hurther, D. & Lemmin, U. 2001 A correction method for turbulence measurements with a 3-D acoustic Doppler velocity profiler. *J. Atmos. Ocean. Technol.* **18**, 446–458.

Hussain, A. K. M. F. 1983 Coherent structures – reality and myth. *Phys. Fluids* **26**, 2816.

Irwin, H. P. A. H. & Smith, P. A. 1975 Prediction of the effect of streamline curvature on turbulence. *Phys. Fluids* **18**, 624–630.

von Kármán, T. 1934 Some aspects of the turbulence problem. *Intl Congr. Appl. Mech. Cambridge*, p. 54.

Komori, S., Ueda, H., Ogino, F. & Mizushina, T. 1983 Turbulence structure in stably stratified open-channel flow. *J. Fluid Mech.* **130**, 13–26.

Lemmin, U. & Rolland, T. 1997 Acoustic velocity profiler for laboratory and field studies. *J. Hydraul. Engng ASCE*, **123**, 1089–1098.

McBean, G. A. & Miyake, M. 1972 Turbulent transfer mechanisms in the atmospheric surface layer. *Q. J. R. Met. Soc.* **98**, 383–398.

Odgaard, A. J. 1984 Bank erosion contribution to stream sediment load. *IIHR Rep.* 280, Iowa Inst. Hydraul. Res. Iowa.

Prandtl, L. 1930 Reprinted in *L. Prandtl gesammelte Abhandlungen 2*, p. 778, 1961.

Prandtl, L., Oswatitsch, K. & Wieghardt, K. 1990 *Führer durch die Strömungslehre*, 9th edn. Vieweg, Braunschweig.

Rolland, T. 1994 Développement d'une instrumentation Doppler ultrasonore: application aux écoulements turbulents en hydraulique. PhD thesis 1281, Ecole Polytechnique Fédérale Lausanne, Switzerland.

So, R. M. C. & Mellor, G. L. 1973 Experiment on convex curvature effects in turbulent boundary layers. *J. Fluid Mech.* **60**, 43–62.

Tamburrino, A. & Gulliver, J. S. 1999 Large flow structures in a turbulent open channel flow. *J. Hydraul. Res.* **37**, 363–380.